REGULAR ARTICLE

Ab initio theoretical study of luminescence properties of Pr³⁺-doped Lu₂O₃

José Luis Pascual · Zoila Barandiarán ·
Luis Seijo

Abstract Ab initio embedded cluster calculations have been performed on Pr³⁺-doped Lu₂O₃, in order to investigate the mechanism responsible for the highly efficient $^3P_0 \rightarrow {}^1D_2$ non-radiative relaxation experimentally observed. $(PrO_6)^{9-}$ embedded clusters representing the C_2 and S_6 substitutional sites of Pr³⁺:Lu₂O₃ have been studied using wave function-based methods. It is found that an outward relaxation of the first coordination sphere around the impurity takes place upon doping. At the relaxed geometry of the lowest spin triplet $4f5d$ state, all the $4f5d$ states lie much higher in energy than all $4f^2$ states (except the ^1S multiplet). This result is in opposition to the interpretation of intersystem crossing through a low-lying $4f5d$ excited state of Pr³⁺ as the mechanism for the fast non-radiative $^3P_0 \rightarrow {}^1D_2$ relaxation proposed in the literature. Absorption to the lowest spin triplet $4f5d$ state is calculated to be around 4,800 cm⁻¹ higher for the C_2 site than for the S_6 site, supporting the assignment of bands in the excitation spectrum previously reported.

J. L. Pascual
Departamento de Química Física Aplicada,
Universidad Autónoma de Madrid, 28049 Madrid, Spain

Z. Barandiarán · L. Seijo
Departamento de Química, Universidad Autónoma de Madrid,
28049 Madrid, Spain

Z. Barandiarán · L. Seijo (✉)
Instituto Universitario de Ciencia de Materiales Nicolás Cabrera,
Universidad Autónoma de Madrid, 28049 Madrid, Spain
e-mail: luis.seijo@uam.es

1 Introduction

Pr³⁺-doped ionic solids are a useful class of phosphors. The electronic structure of the ion can give rise to luminescence in the ultraviolet (UV), visible, and infrared (IR) wavelength ranges. Some Pr³⁺-doped fluorides have been investigated as promising candidates for luminescence lamps due to the fact that they exhibit photon cascade emission [1]. Praseodymium-doped oxides have been considered as potential lasers in the visible and IR domains [2].

Another important application is as phosphors in fast decay scintillators for X-ray computed tomography. For example, Gd_2O_2S:Pr has been used to that end [3, 4]. The predominant radiative transitions of Pr³⁺ (ground electronic configuration $4f^2$) upon X-ray excitation occur from the $^3P_0$ and $^1D_2$ excited levels to the $^3H_4$ ground level. The $^3P_0 \rightarrow {}^3H_4$ transition exhibits a very short decay time (in the μs scale) while the $^1D_2 \rightarrow {}^3H_4$ transition is slower (decay time in the ms scale) [5, 6]. As decay times much faster than the response times of the detector systems are required for scintillators [3], phosphors that exhibit transitions only from the $^3P_0$ are preferred for X-ray computed tomography. $^3P_0 \rightarrow {}^1D_2$ non-radiative transitions are key factors in the suitability of the materials as fast decay scintillators. Knowledge of the mechanisms of non-radiative transitions is important for the proper design of this kind of materials.

Following this line, experimental studies have been performed to gain a better understanding of these mechanisms in Pr³⁺-doped solids. Pr³⁺-doped rare earth

sesquioxides, especially yttrium sesquioxide, form a family of compounds that have been studied in relation to their luminescence properties [2, 5–8]. Depending on the crystal symmetry and substitution site, Pr^{3+}-doped rare earth sesquioxides are found to emit preferentially from the $^3P_0$ state (hexagonal phases, monoclinic phases with high coordination) or from the $^1D_2$ state (monoclinic phases with low coordination, cubic phases) [8].

DeMello Donegá et al. [6] have studied the mechanisms that contribute to Pr^{3+} $^3P_0 \rightarrow {}^1D_2$ non-radiative relaxation in a large number of oxide hosts, including lutetium sesquioxide (Lu_2O_3). Several mechanisms are taken into account in their study: [6] (1) multiphonon relaxation; (2) cross-relaxation within pairs of Pr^{3+} ions; (3) intersystem crossing through a low-lying $4f5d$ excited state of Pr^{3+}; (4) intersystem crossing through a low-lying Pr-to-metal charge transfer state. A fifth mechanism, relaxation through Pr^{3+}-trapped exciton states, has been invoked to explain the quenching of the $^3P_0$ luminescence in Pr^{3+}-doped $LiNbO_3$ [9] and the different behavior of Pr^{3+}-doped $LiNbO_3$ and $LiTaO_3$ [10]. Intersystem crossing through Pr-to-metal charge transfer states, sometimes referred to as *virtual recharge* mechanism, has been extensively invoked to explain the luminescent properties of a number of Pr-doped hosts containing complex oxoanions, such as titanates, vanadates, and niobates (e.g. see Refs. [11, 12] and references therein).

The spectral properties of Pr^{3+}-doped Lu_2O_3 were experimentally investigated by DeMello Donegá et al. [6]. They recorded excitation and emission spectra, and from them, they obtained estimations of the radiative and non-radiative decay constants. They observed that cubic Lu_2O_3:Pr^{3+} emits only from the $^{-1}D_2$ state. The fact that lowest $4f5d$ excited states lie around $36{,}000\ cm^{-1}$, that is, relatively low in energy, suggested that the dominant mechanism for the very highly efficient $^3P_0 \rightarrow {}^1D_2$ non-radiative relaxation could be intersystem crossing through the $4f5d$ excited states of Pr^{3+} [6]. In order to account for the different experimental observations, the authors tentatively proposed a configurational coordinate diagram (Fig. 7 in Ref. [6]) for the system. The main features of this diagram were that the force constant of the $4f5d$ excited state is much greater than that of the $4f^2$ states and that the energy of the relaxed $4f5d$ excited state lies between the $^3P_0$ and $^1D_2$ levels ($4f^2$). A shortening of the Pr-O distances upon doping is invoked to explain these facts. The validity of these hypothesis can be checked in ab initio quantum mechanical calculations, which is one of the objectives of this work.

In this paper, we present theoretical ab initio calculations on the electronic structure of Pr^{3+}-doped Lu_2O_3. We have performed spin-free ab initio model potential (AIMP) embedded cluster optimizations of the geometry in relevant

electronic states, and then, we have calculated vertical transition energies at the optimal geometries. The AIMP embedded cluster method [13, 14] has been successfully applied in a number of structural and spectroscopical studies of lanthanide and actinide-doped ionic hosts [15–20]. As a result of the calculations, we obtain the local distortion produced by the Pr^{3+} doping, and we give support to the assignments of the absorption bands to Pr^{3+} occupying different sites in the Lu_2O_3 lattice [5, 6]. The energy minima of the lowest $4f5d$ states are calculated and located with respect to the $4f^2$ $^3P_0$ and $^1D_2$ levels, and possible luminescence after $4f \rightarrow 5d$ excitation is predicted. In spite of the computational demands required by the theoretical results presented here, this paper is only a first step into the elucidation of the electronic structure of the Pr^{3+} defect in cubic rare earth sesquioxides. Further calculations on more complicated mechanisms such as the *virtual recharge* mechanism and intersystem crossing through Pr^{3+}-trapped exciton states are underway in our laboratory.

The paper is organized as follows: in Sect. 2, we briefly describe the method used together with the details of the calculations. The results of the calculations are presented in Sect. 3, and a discussion of them is presented in Sect. 4. We present the conclusions in Sect. 5.

2 Method

2.1 Structure of the Lu_2O_3 host

The crystal structure of Lu_2O_3 is of the rare earth sesquioxide C-type structure, the bixbyite structure, cubic with space group $Ia\bar{3}(T_h^7)$ [21] (see Fig. 1). The lattice parameter of Lu_2O_3 is $a_0 = 10.931\ \text{Å}$. In the bixbyite structure, there are two crystallographically different cations sites. In Lu_2O_3, 24 Lu^{3+} cations occupy the Wyckoff position 24d at $(u, 0, 1/4)$, and 8 Lu^{3+} cations occupy the Wyckoff position 8b at $(1/4, 1/4, 1/4)$. The oxygen atoms occupy the general 48e position at (x, y, z). The coordination polyhedra are distorted cubes, in which six corners are occupied by oxygen ions and the remaining two are vacant. The resulting coordination polyhedra around both cations are depicted in Fig. 2. In the case of the Lu^{3+} 24d ions, the vacant sites are located along a face diagonal of the cube, leading to site symmetry C_2. In the case of the Lu^{3+} 8b ions, the two oxygens are missing along the body diagonal of the cube, and the resulting site symmetry is S_6 (or C_{3i}). The internal parameters of Lu_2O_3 have not been experimentally determined to our knowledge. Instead, they have been obtained by periodic density-functional theory calculations using the generalized-gradient approximation, as
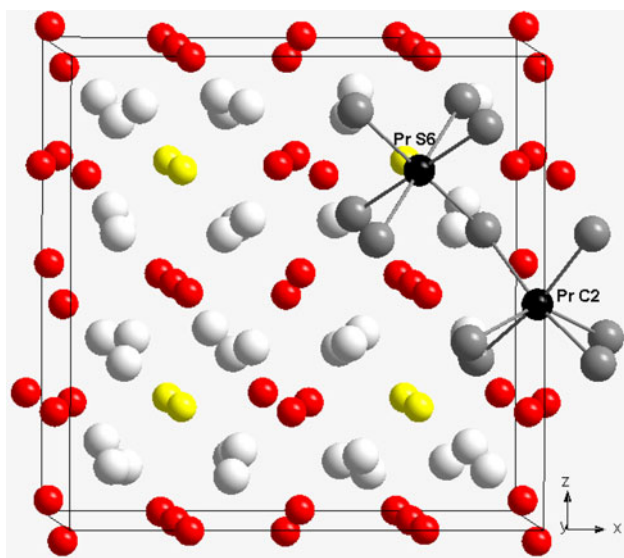
Fig. 1 Cubic cell of the bixbyite structure showing the C_2 and S_6 coordination polyhedra around the dopant ion
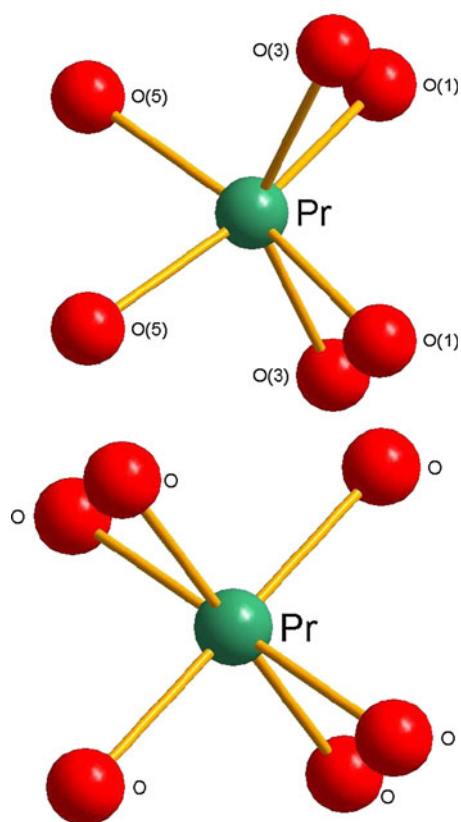
Fig. 2 Schematic representation of the C_2 and S_6 coordination polyhedra around the cations in the bixbyite structure

reported in Ref. [22]. The resulting internal parameters are as follows: $u = -0.0330$, $x = 0.3912$, $y = 0.1521$, and $z = 0.3800$. In the C_2 site, there are three pairs of

Table 1 Lu–O and Pr–O equilibrium distances for the C_2 and S_6 polyhedra in the Lu_2O_3 and $Lu_2O_3 : Pr^{3+}$ crystals, respectively

	Lu–O	Pr–O	
		$4f^2$	$4f5d$
C_2 site			
O(1)	2.289	2.343 (0.054)	2.335
O(3)	2.223	2.294 (0.071)	2.295
O(5)	2.200	2.225 (0.025)	2.201
O(avg.)	2.237	2.287 (0.050)	2.277
S_6 site			
O	2.239	2.302 (0.063)	2.280
Mismatch of ionic radii		0.13[a]	

Lu–O distances have been taken from Ref. [22]. Pr–O distances have been optimized for the lowest spin triplet $4f^2$ and $4f5d$ states at the CASSCF level in this work. Lattice distortions produced by the Pr^{3+} impurity in parenthesis. All distances in Å

[a] Radii taken from Ref. [40]

neighboring oxygen ions at three different distances, in the S_6 site all six oxygen ions are at the same distance. These perfect lattice data are summarized in Table 1.

The ratio of C_2 to S_6 sites in 3:1. It is believed that, when an impurity substitutes for a lattice cation in cubic sesquioxides, it enters both crystallographic sites [5] and spectral features have been interpreted in the literature [5, 6] assuming this, as commented below. Stanek et al. [23] have studied the site preference of trivalent dopant ions in bixbyite sesquioxides, by atomic-scale simulations using classic pair potentials, and they have found a marked preference for S_6 site substitution in $Pr^{3+} : Lu_2O_3$. In this work, we have studied both substitutional sites.

2.2 Details of the calculations

The local geometries around the Pr^{3+} ion and the transition energies reported in this work have been calculated using embedded cluster wave function-based methods. For this purpose, $(PrO_6)^{9-}$ clusters were embedded in ab initio model potential (AIMP) [13, 14] representations of the pure Lu_2O_3 host. The clusters chosen to model the C_2 and S_6 sites are shown on Fig. 2. AIMP total ion embedding potentials, calculated in this work, were located at the perfect Lu_2O_3 ionic positions. They accurately reproduce the quantum mechanical interactions between the external crystal ions (Lu^{3+} and O^{2-} ions) and the wave functions associated with the point defect $(PrO_6)^{9-}$ clusters. They include electrostatic (Coulomb and short range corrections), exchange, and Pauli repulsion interactions, and they have been produced using the recipes of Refs. [13, 14]. Embedding AIMPs were used at all lattice ions located within a cube of length $3a_0$ centered at the impurity site. The remaining ions within a cubic shell of length $5a_0$ are

treated as point charges, and Evjen's method [24] is used to define the charge of the frontier ions.

Bonding, static, and dynamic correlation, and scalar relativistic effects within the $(PrO_6)^{9-}$ clusters have been taken into account by performing state-averaged complete active space self-consistent field (SA-CASSCF) [25–27] and multistate second order perturbation theory (MS-CASPT2) [28–31] calculations using a scalar relativistic many-electron Hamiltonian. The relativistic effective [Kr]-core model potential and $(14s10p10d8f3g)/[6s5p6d4f1g]$ Gaussian valence basis set, taken from Refs. [32, 33], were used for Pr. The [He]-core effective core potential and $(5s6p1d)/[3s4p1d]$ Gaussian valence basis set, taken from Ref. [34], were used for oxygen, extended with one p-type diffuse function for anion [35] and one d-type polarization function. [36] Spin–orbit coupling has not been included in the calculations; thus, comparison with experimental data is semiquantitative. As we show below, inclusion of spin–orbit effects should not alter the conclusions of this work. These calculations were performed using the program MOLCAS [37]. All the model potentials (core and embedding) and basis sets used in this work are available from the authors [38].

In a first step, the geometry of the clusters was optimized at the CASSCF level. The CAS space was chosen so that it comprises all configurations in which two electrons occupy the thirteen molecular orbitals of main character Pr $4f$, Pr $5d$, and Pr $6s$. In the case of the S_6 site, we performed the calculations using C_i symmetry. The molecular orbitals were chosen so as to minimize the average energy of all states with dominant $4f^2$ (21 ^3A_g states, 28 ^1A_g states) or $4f5d$ and $4f6s$ configurational character (42 ^3A_u states, 42 ^1A_u states). The cluster geometry was optimized for the 1 ^3E_g state (lowest spin triplet $4f^2$ state) and the 1 ^3A_u state (lowest spin triplet $4f5d$ state). The resulting optimized geometries were very nearly S_6 symmetric.

In the case of the C_2 site, we performed the calculations without any symmetry (point group C_1). The molecular orbitals were chosen so as to minimize the average energy of all states with dominant $4f^2$, $4f5d$, and $4f6s$ configurational character (63 ^3A states, 70 ^1A states). The cluster geometry was optimized for the 1 ^3B state (lowest spin triplet $4f^2$ state) and the 13 ^3B state (lowest spin triplet $4f5d$ state). The resulting optimized geometries were very nearly C_2 symmetric.

We have calculated the vertical transition energies at the CASSCF $4f^2$ and $4f5d$ optimized geometries using the MS-CASPT2 method. A total of 58 electrons, which occupy the orbitals with main character Pr $5s$, $5p$, $4f$, $5d$, and $6s$ (10 electrons) and O $2s$, $2p$ (48 electrons), have been correlated. An imaginary shift [39] of 0.10 au. has been used in the calculations to ensure that no intruder states are present. Large and uniform weights of the reference wave functions (around 70%) were found in the CASPT2 calculations. We will refer to these calculations as MS-CASPT2(O48,Pr10).

3 Results

3.1 Local distortions

We present the optimized Pr–O distances for the lowest $4f^2$ and $4f5d$ spin triplet states both at the C_2 and S_6 sites in Table 1 together with the geometry of the perfect Lu_2O_3 lattice calculated at Ref. [22]. First, it can be seen that, upon doping, the Pr–O distances are larger than in the perfect lattice, for both sites. This result is totally in line with previous calculations performed in similar systems: the results upon doping qualitatively reflect the mismatch of ionic radii between the dopant ion and the substituted host ion and are quantitatively smaller. In this case, the radii are 0.86 Å for Lu^{3+} and 0.99 Å for Pr^{3+} (both in coordination number 6) [40].

The Pr-O distances shorten by about 0.01 Å at the C_2 site and by about 0.02 Å at the S_6 site upon $4f \rightarrow 5d$ excitation. In the case of the C_2 site, the different Pr–O distances behave differently: two of them (Pr–O(1) and Pr–O(5)) shorten while the third one (Pr–O(3)) remains essentially unchanged. This shortening is in agreement with what has been found in other lanthanides and actinides in high-symmetry halide coordination [15, 16, 18, 20, 41], and recently has been experimentally concluded [42]. An extensive study of the factors leading to this result for several ions, including Pr^{3+}, can be found in Ref. [43]. Recent results on Ce^{3+}-doped YAG [17] show that this shortening upon excitation is also found in the case of lower symmetry sites. Our results for Pr^{3+}-doped Lu_2O_3 are in line with these latter results.

The calculation of the optimized geometries does not include spin–orbit nor electron correlation effects. The effect of the lack of spin–orbit in the structures should be negligible, in the line of what we have found in similar systems [16, 18]. The only exception is those systems and states in which spin–orbit coupling mixes states belonging to different dominant electron configurations [20]. This is not the case here, as the separation between the relevant $4f^2$ and $4f5d$ manifolds is large (see below).

The effect of the inclusion of electron correlation in the geometry optimization should be a uniform shortening of less than 0.02 Å in the equilibrium distances [44]. This additional shortening does not change the main conclusion of this section, viz. the outward distortion of the clusters caused by doping in the $Pr^{3+}:Lu_2O_3$ lattice.

3.2 Relative energies of the $4f^2$ and $4f5d$ manifolds

Table 2 presents vertical transition energies of the $(PrO_6)^{9-}$ embedded clusters, with respect to the $4f^2$ ground state, at different cluster geometries, for the C_2 site and the

Table 2 Vertical transition energies of the $(PrO_6)^{9-}$ embedded cluster calculated at the C_2 and S_6 sites

	C_2 cluster geometry				S_6 cluster geometry	
	Perfect lattice	Relaxed $4f^2$	Relaxed $4f5d$		Relaxed $4f^2$	Relaxed $4f5d$
$4f^2$ *manifold*						
From ^3H						
$1\,^3B$	0	0	0	$1\,^3E_g$	0	0
$2\,^3B$	100	275	180	$1\,^3A_g$	95	110
$1\,^3A$	150	280	325	$2\,^3E_g$	610	640
$2\,^3A$	630	745	750	$2\,^3A_g$	800	815
$3\,^3B$	810	895	915	$3\,^3A_g$	1,130	1,205
$3\,^3A$	840	960	1,030	$3\,^3E_g$	1,250	1,325
$4\,^3A$	1,255	1,215	1,215	$4\,^3E_g$	1,980	2,125
$4\,^3B$	1,455	1,467	1,530			
$5\,^3B$	1,730	1,715	1,755			
$5\,^3A$	1,795	1,830	1,905			
$6\,^3B$	1,865	1,870	1,900			
From ^3F						
$6\,^3A$	4,385	4,390	4,410	$4\,^3A_g$	4,800	4,845
$7\,^3B$	4,810	4,775	4,815	$5\,^3E_g$	5,325	5,440
$8\,^3B$	4,920	5,015	5,125	$5\,^3A_g$	5,355	5,405
$9\,^3B$	5,095	5,185	5,235	$6\,^3E_g$	5,780	5,925
$7\,^3A$	5,195	5,190	5,180	$6\,^3A_g$	6,075	6,205
$8\,^3A$	5,365	5,330	5,350			
$10\,^3B$	5,690	5,590	5,640			
From ^1G						
$1\,^1B$	5,645	5,835	5,825	$1\,^1E_g$	5,540	5,530
$1\,^1A$	5,715	5,560	5,615	$1\,^1A_g$	5,655	5,685
$2\,^1B$	5,805	6,013	6,005	$2\,^1A_g$	5,895	5,910
$2\,^1A$	5,905	6,045	6,075	$2\,^1E_g$	6,095	6,110
$3\,^1B$	6,380	6,495	6,505	$3\,^1E_g$	7,065	7,155
$3\,^1A$	6,760	6,300	6,330	$3\,^1A_g$	7,645	7,750
$4\,^1A$	7,035	7,170	7,225			
$5\,^1A$	7,560	7,495	7,560			
$4\,^1B$	7,760	7,675	7,735			
From ^1D						
$6\,^1A$	14,400	14,595	14,525	$4\,^1E_g$	15,685	15,650
$7\,^1A$	14,910	15,255	15,300	$4\,^1A_g$	16,357	16,410
$5\,^1B$	15,395	15,475	15,520	$5\,^1E_g$	17,480	17,555
$6\,^1B$	16,315	16,385	16,390			
$8\,^1A$	16,520	16,515	16,550			
From ^3P						
$11\,^3B$	18,985	19,220	19,280	$7\,^3E_g$	22,665	22,675
$12\,^3B$	20,875	21,220	21,335	$7\,^3A_g$	23,840	23,985
$9\,^3A$	21,395	21,435	21,365			
From ^1I						
$9\,^1A$	20,285	20,760	20,700	$5\,^1A_g$	21,070	20,985
$7\,^1B$	20,735	21,035	21,100	$6\,^1A_g$	21,530	21,485

Table 2 continued

	C_2 cluster geometry				S_6 cluster geometry	
	Perfect lattice	Relaxed $4f^2$	Relaxed $4f5d$		Relaxed $4f^2$	Relaxed $4f5d$
$10\,^1A$	20,865	21,150	21,150	$6\,^1E_g$	21,575	21,505
$8\,^1B$	20,945	21,375	21,300	$7\,^1E_g$	21,650	21,575
$11\,^1A$	21,540	21,540	21,660	$7\,^1A_g$	22,125	22,155
$9\,^1B$	21,730	21,970	22,190	$8\,^1E_g$	23,430	23,495
$12\,^1A$	22,295	22,305	22,105	$9\,^1E_g$	24,375	24,545
$10\,^1B$	22,355	22,430	22,380	$8\,^1A_g$	24,515	24,780
$11\,^1B$	22,395	22,550	22,670	$9\,^1A_g$	24,560	24,850
$13\,^1A$	22,735	22,650	22,595			
$14\,^1A$	23,180	23,090	22,985			
$15\,^1A$	24,955	25,125	25,280			
$12\,^1B$	25,065	25,205	25,340			
From ^1S						
$19\,^1A$	40,840	41,680	41,690	$10\,^1A_g$	46,345	46,365
$4f^1\,5d^1$ *manifold (up to* $50,000\,\mathrm{cm}^{-1}$)						
Spin triplet states						
$13\,^3B$	38,105	38,690	38,250	$1\,^3A_u$	33,860	32,800
$10\,^3A$	38,375	39,220	38,740	$2\,^3A_u$	34,680	33,690
$11\,^3A$	38,980	40,125	39,485	$1\,^3E_u$	34,720	33,740
$14\,^3B$	39,840	39,840	39,530	$2\,^3E_u$	36,505	35,540
$15\,^3B$	39,895	40,280	39,840	$3\,^3A_u$	36,550	35,790
$16\,^3B$	40,130	40,690	40,970	$3\,^3E_u$	37,795	37,490
$17\,^3B$	40,400	41,275	41,405	$4\,^3A_u$	38,405	38,235
$12\,^3A$	40,590	41,420	41,330	$4\,^3E_u$	38,905	38,725
$13\,^3A$	40,975	41,935	41,560	$5\,^3A_u$	39,100	38,850
$18\,^3B$	41,210	41,665	41,830	$5\,^3E_u$	40,480	40,280
$14\,^3A$	41,260	42,130	41,910	$6\,^3A_u$	41,205	40,950
$19\,^3B$	41,515	42,200	42,570	$7\,^3A_u$	41,280	41,090
$15\,^3A$	41,790	42,390	42,395	$6\,^3E_u$	41,640	41,420
$16\,^3A$	42,395	43,535	43,565	$7\,^3E_u$	42,950	42,950
$20\,^3B$	42,710	43,335	43,340			
$21\,^3B$	42,800	43,680	43,795			
$22\,^3B$	43,930	44,700	44,940			
$17\,^3A$	44,085	44,615	44,265			
$18\,^3A$	44,475	45,080	44,925			
$23\,^3B$	44,755	45,150	45,030			
$19\,^3A$	44,860	45,700	45,940			
Spin singlet states						
$16\,^1A$	37,235	37,815	37,405	$1\,^1A_u$	33,770	33,120
$13\,^1B$	37,630	38,070	37,560	$1\,^1E_u$	34,665	33,900
$14\,^1B$	38,460	38,975	38,590	$2\,^1A_u$	35,340	34,490
$17\,^1A$	39,550	40,030	39,560	$2\,^1E_u$	35,715	34,965
$18\,^1A$	39,655	40,200	39,830	$3\,^1E_u$	37,870	37,570
$15\,^1B$	40,340	41,170	40,930	$3\,^1A_u$	38,555	38,115
$16\,^1B$	41,640	42,055	41,330	$4\,^1A_u$	39,360	38,540
$20\,^1A$	41,770	42,355	42,170	$4\,^1E_u$	42,040	41,690

Table 2 continued

	C_2 cluster geometry				S_6 cluster geometry	
	Perfect lattice	Relaxed $4f^2$	Relaxed $4f5d$		Relaxed $4f^2$	Relaxed $4f5d$
$21\,^1A$	41,930	42,550	42,355	$5\,^1A_u$	42,440	42,300
$17\,^1B$	42,370	43,220	42,490	$5\,^1E_u$	42,590	42,360
$18\,^1B$	42,485	43,530	43,850	$6\,^1A_u$	42,775	42,510
$22\,^1A$	43,510	44,220	44,005	$6\,^1E_u$	43,260	43,010
$23\,^1A$	43,740	44,315	44,290	$7\,^1A_u$	46,480	46,220
$19\,^1B$	43,755	44,355	44,280	$7\,^1E_u$	46,965	46,720
$20\,^1B$	44,405	45,075	45,055			
$24\,^1A$	44,500	45,230	45,085			
$25\,^1A$	45,240	46,395	46,430			
$21\,^1B$	45,385	46,455	46,400			
$22\,^1B$	47,105	48,100	48,160			
$26\,^1A$	47,850	48,900	49,055			
$23\,^1B$	48,450	48,860	48,850			
$4f^1 5d^1 + 4f^1 6s^1$ *manifold*						
Spin triplet states						
$20{-}22\,^3A, 24{-}27\,^3B$	58,355–60,950	58,810–61,225	57,820–60,350	$8{-}11\,^3A_u, 8{-}12\,^3E_u$	71,670–76,230	72,215–76,925
$23{-}29\,^3A, 28{-}34\,^3B$	75,025–79,610	75,770–79,965	76,775–80,750	$12{-}14\,^3A_u, 13{-}14\,^3E_u$	82,330–85,830	80,650–84,370
Spin singlet states						
$27{-}29\,^1A, 24{-}27\,^1B$	59,170–63,300	59,410–63,570	58,430–62,745	$8{-}11\,^1A_u, 8{-}12\,^1E_u$	71,085–82,100	71,695–80,240
$30{-}36\,^3A, 28{-}34\,^1B$	74,005–83,880	75,580–85,520	76,075–85,460	$12{-}14\,^1A_u, 13{-}14\,^1E_u$	82,880–86,405	81,755–84,925

Transition energies calculated at the C_2 site using the perfect Lu_2O_3 lattice, relaxed $1\,^3B$–$4f^2$ and relaxed $13\,^3B$–$4f5d$ cluster geometries. Transition energies calculated at the S_6 site using the relaxed $1\,^3E_g$–$4f^2$ and relaxed $1\,^3A_u$–$4f5d$ cluster geometries. The calculations include 58 valence electron correlation, static relativistic effects and Lu_2O_3 embedding host effects. (MS-CASPT2(O48,Pr10) level) All numbers are in cm^{-1}

S_6 site. For each cluster, we have calculated the vertical transition energies at the $4f^2$ ground-state equilibrium geometry and at the optimal geometry of the lowest spin triplet $4f5d$ state. Vertical transition energies have also been calculated at the geometry of the perfect Lu_2O_3 lattice for the C_2 site. All the transition energies have been computed at the MS-CASPT2(O48,Pr10) level. The data in the table are also shown in Fig. 3. The electronic states are grouped according to their main $4f^2$, $4f5d$, or $4f6s$ configurational character. Such a distinction is done by inspection of the wave functions and symmetry (g/u) considerations.

The $4f^2$ manifold spans 25,000 cm^{-1} in both sites, the only exception being the state related to the $4f^2$-^1S multiplet, which lies at much higher energy and is inmersed in the $4f5d$ electronic manifold. It can be seen that the vertical transition energies to the ^3F,^1G, and ^1I multiplets are very similar for both sites, but the rest of the multiplets lies at lower energies in the C_2 site than in the S_6 site: 1,100 cm^{-1} for ^1D, 3,300 cm^{-1} for ^3P, and 4,700 cm^{-1} for ^1S.

The $4f5d$ manifold, both for the C_2 and S_6 sites, appears to be well above the $4f^2$ states. The $4f^2$-$4f5d$ energy gap is 13,500 cm^{-1} in the C_2 site and 9,300 cm^{-1} in the S_6 site. Relaxation of the geometry of the lowest spin triplet $4f5d$ states does not modify this picture. Relaxation energies are 450 cm^{-1} and 1,050 cm^{-1} for the C_2 and S_6 sites, respectively.

The $4f5d$ manifolds show different submanifold structure in the two sites due, basically, to the different crystal field splitting of the excited 5d electron. The centroids of the $4f5d$ levels are at 52,670 cm^{-1} and 52,600 cm^{-1}, and the difference between the lowest level and the centroids is 15,005 and 18,740 cm^{-1} (S_6). These data suggest that the ligand field effects are larger in the S_6 site.

The vertical transition energies presented in Table 2 do not include indirect effects of dynamic correlation through the optimized geometries, since the optimization has been done at the CASSCF level. As commented above, a systematic bond length shortening should be expected as a consequence of dynamic correlation effects [44]. An estimation of such indirect effect can be deduced by comparing the transition energies evaluated at the perfect lattice geometry and at the $4f^2$ ground-state relaxed geometry for
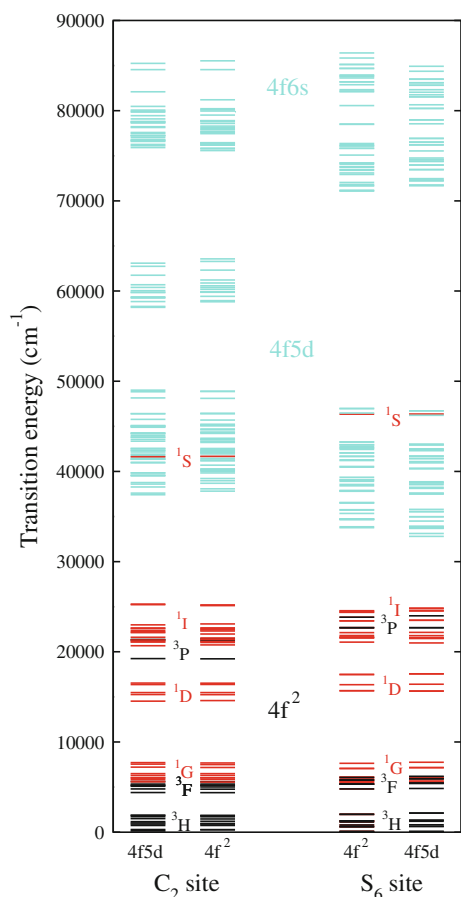
Fig. 3 Energy levels of $Pr^{+3} : Lu_2O_3$ as calculated in this work. Energy levels are calculated at the relaxed $4f^2$ and $4f5d$ geometries, both for C_2 and S_6 sites. All numbers are calculated at the MS-CASPT2 level

the C_2 site, since the bond lengths are shorter in the former structure. This comparison allows to conclude that the indirect effect of dynamic correlation is not significant and, more important for the objective of this work, does not alter the energy gaps between the $4f^2$ and $4f5d$ manifolds.

Spin–orbit coupling is also absent in the calculations of the vertical transition energies. Yet, previous calculations on a very similar system like Ce^{3+}-doped YAG [17] show that spin–orbit effects decrease the $4f-5d$ energy gap by less than 550 cm^{-1}. Thus, spin–orbit coupling cannot be expected to reduce the calculated $4f^2-4f5d$ energy gap so as to locate the lowest $4f5d$ states within the $4f^2$ manifold.

4 Discussion

We discuss here the local distortion produced by the Pr^{3+} impurity, the possibility of intersystem crossing through $4f5d$ excited states, and some observed spectral features of Pr^{3+}-doped Lu_2O_3 using the results of Sect. 3.

We focus first on the distortion of the Lu_2O_3 lattice due to the Pr^{3+} impurity. An inward distortion due to strong Pr–O orbital mixing has been suggested [6], in order to account for the spectral features of the material. The present calculations lead to an outward distortion of the first coordination sphere that is smaller than suggested by the mismatch of ionic radii due to strong metal-ligand mixing.

This inward distortion was invoked in relation to the extremely fast Pr^{3+} non-radiative relaxation found in the material. This relaxation has been suggested to be due to intersystem crossing through low-lying $4f5d$ states. A configurational coordination diagram to account for the relaxation has been presented [6] where the $4f5d$ minimum energy lies below the $^3P_0$ level and above and close to the $^1D_2$ level, which would provide a path for $^3P_0 \rightarrow {}^1D_2$ non-radiative relaxation. The present ab initio results show that the energy of the lowest $4f5d$ states is well above all the $4f^2$ (except the state related to ^1S-$4f^2$, as we commented above) even after excited state relaxation is considered, and they do not support intersystem crossing through $4f5d$ states as the quenching mechanism. Other mechanisms should be investigated in order to explain the high non-radiative decay rate found in Ref. [6].

We will focus now on the different spectral features that have been reported in Ref. [6]. As we commented above, the lack of spin–orbit effects in our calculations allows to make only semiquantitative comparisons with experimentally determined spectral features. This fact is more severe for $f-f$ transitions than for $f-d$, as the former should be more influenced by spin–orbit coupling. The emission and excitation spectra of Pr^{3+}:Lu_2O_3 have been reported in Ref. [6]. In the excitation spectra, several lines are reported between 16,600 and 17,540 cm^{-1}, assigned to excitations to the ^1D multiplet levels; another group of lines between 20,000 and 23,800 cm^{-1} is assigned to $^3H \rightarrow {}^3P, {}^1I$ transitions. The calculations show a good semiquantitative agreement with these data. The position of the $^3H_4 \rightarrow {}^3P_0$ zero-phonon line is reported to be 19,996 cm^{-1}; the present calculation for the lowest $^3H \rightarrow {}^3P$ transition in C_2 site (the most frequent site) is 19,220 cm^{-1}. The gap between the $^1D_2$ and the $^3P_0$ levels is reported to be 2,600 cm^{-1} whereas we predict 2,700 cm^{-1}; spin–orbit splitting of the $^3P_0$-related levels is expected to lower the theoretical gap and to lead, perhaps, to a certain underestimation when spin–orbit coupling is considered. The crystal field splitting of the $^1D_2$ multiplet is found to be 1,280 cm^{-1}, and our data slightly overestimate it (1,920 cm^{-1}, site C_2; 1,800 cm^{-1}, site S_6); spin–orbit coupling is not expected to be important in this.

A broad band, with a maximum at 36,200 cm^{-1} and a shoulder at 30,300 cm^{-1}, is reported in the excitation

spectra. By comparison with other measurements on Pr^{3+}:Lu_2O_3 (Ln = Y, Sc, Gd) [5], they are ascribed to $4f^2 \rightarrow 4f5d$ transitions within Pr^{3+} ions at C_2 and S_6 sites in Lu_2O_3, respectively. This is in contrast with the conclusions of the pair-potential studies [23], that predict only S_6 substitution in this lattice. According to the present calculations, the lowest $4f^2 \rightarrow 4f5d$ (triplet states) excitation energies are 38,690 and 33,860 cm^{-1} for the C_2 and S_6 sites, respectively. Thus, the ab initio calculations support the assignment done in Ref. [6] of the higher energy band to the Pr^{3+} ions occupying the C_2 site and the shoulder to Pr^{3+} ions occupying the S_6 site.

Both for C_2 and S_6 sites, there is a large gap in energy between the highest level of the $4f^2$ manifold and the lowest level of the $4f5d$ manifold. At the lowest spin triplet $4f5d$ geometry, this gap amounts 12,900 cm^{-1} for the C_2 site and 8,000 cm^{-1} for the S_6 site. The highest lying ^1S multiplet is inmersed in the $4f5d$ manifold in both sites. The lowest spin triplet $4f5d$ state should be metastable, and emission from it should be expected under $4f5d$ excitation. However, no such emission is experimentally observed [6]. Instead, identical emission is found under $^3P_0$ excitation and under $4f5d$ excitation [6]. Thus, some mechanism should exist in the material for efficient non-radiative $4f5d \rightarrow {}^1D_2$ relaxation. This mechanism is likely to be the same that provides a fast $^3P_0 \rightarrow {}^1D_2$ relaxation.

5 Conclusions

We have performed ab initio model potential calculations of the electronic structure of $(PrO_6)^{9-}$ embedded clusters that represent the C_2 and S_6 sites of Pr^{3+}-doped lutetium sesquioxide. We have performed spin-free CASSCF optimizations of the geometry around the Pr^{3+} impurity, and at the equilibrium geometries of the $4f^2$ and $4f5d$ lowest spin triplet states, we have performed MS-CASPT2 calculations of the vertical transition energies from the ground state to all the states coming from the $4f^2$, $4f5d$, and $4f6d$ manifolds, both for spin triplet and singlet. As a result of the geometry optimization, we find an outward distortion of the first coordination shell around the impurity upon doping. The transition energy from the minimum of the lowest $4f5d$ state is found to be well above the position of both $^3P_0$ and $^1D_2$ levels (around 10,000 cm^{-1}), strongly suggesting that intersystem crossing through this $4f5d$ state is not the dominant mechanism for $^3P_0 \rightarrow {}^1D_2$ non-radiative relaxation. The calculations also predict strong $4f5d \rightarrow 4f^2$ luminescence under $4f5d$ excitation. However, this luminescence is absent in the experimental results [6], suggesting that some mechanism is quenching it, probably the same mechanism responsible for the $^3P_0$ emission

quenching. Other quenching mechanisms have to be investigated to explain the fast non-radiative relaxation. In this line, calculations in order to investigate the *virtual recharge* mechanism [11, 12] and relaxation via intersystem crossing through trapped exciton states [9, 10] are underway in our laboratory. Finally, the present calculations do support the interpretation of the $4f5d$ band maximum and shoulder found in the excitation spectrum [6] of Pr^{3+}-doped Lu_2O_3 as due to electronic transitions of Pr^{3+} ions located at C_2 and S_6 sites, respectively.

References

1. Kück S, Sokólska I, Henke M, Döring M, Scheffler T (2003) J Lumin 102(103):176
2. Guyot Y, Moncorgé R, Merkle LD, Pinto A, McIntosh B, Verdun H (1996) Opt Mater 5:127
3. Yamada H, Suzuki A, Uchida Y, Yoshida M, Yamamoto H, Tsukuda Y (1989) J Electrochem Soc 136:2713
4. Moses WW (2000) . In: Mikhailin VV (eds) Inorganic scintillators and their applications, SCINT99. Moscow State University, Moscow, p 11
5. Aumüller GC, Köstler W, Grabmaier BC, Frey R (1994) J Phys Chem Solids 55:767
6. de Mello Donegá C, Meijerink A, Blasse G (1995) J Phys Chem Solids 56:673
7. Arai M, Matsuda N, Tamatani M (1993) J Alloys Comp 192:45
8. Okumura M, Tamatani M, Albessard AK, Matsuda N (1997) Jpn J Appl Phys 36:6411
9. Koepke C, Wisniewski K, Dyl D, Grinberg M, Malinowski M (2006) Opt Mater 28:137
10. Gryk W, Dujardin C, Joubert M-F, Ryba-Romanowski W, Malinowski M, Grinberg M (2006) J Phys Condens Matter 18:117
11. Boutinaud P, Mahiou R, Cavalli E, Betinelli M (2006) Chem Phys Lett 418:185
12. Boutinaud P, Pinal E, Oubaha M, Mahiou R, Cavalli E, Betinelli M (2006) Opt Mater 28:9
13. Barandiarán Z, Seijo L (1988) J Chem Phys 89:5739
14. Seijo L, Barandiarán Z (1999) In: Leszczynski J (eds) Computational chemistry: reviews of modern trends, vol 4. World Scientific, Singapore, p 55
15. Barandiarán Z, Seijo L (2003) J Chem Phys 118:7439
16. Ordejón B, Karbowiak M, Seijo L, Barandiarán Z (2006) J Chem Phys 125:074511
17. Gracia J, Seijo L, Barandiarán Z, Curulla D, Niemansverdriet H, van Gennip W (2008) J Lumin 128:1248
18. Sánchez-Sanz G, Seijo L, Barandiarán Z (2009) J Phys Chem A 113:12591
19. Sánchez-Sanz G, Seijo L, Barandiarán Z (2010) J Chem Phys 133:114506
20. Sánchez-Sanz G, Seijo L, Barandiarán Z (2010) J Chem Phys 133:114509
21. Wyckoff RWG (1963) Crystal structures. Wiley, New York
22. Marsella L, Fiorentini V (2004) Phys Rev B 69:172103
23. Stanke CR, McClellan KJ, Uberuaga BP, Sickafus KE, Levy MR, Grimes RW (2007) Phys Rev B 75:134101

24. Evjen HM (1932) Phys Rev 39:675
25. Roos BO, Taylor PR, Siegbahn PEM (1980) Chem Phys 48:157
26. Siegbahn PEM, Heiberg A, Almlöf J, Roos BO (1981) J Chem Phys 74:2384
27. Siegbahn P, Heiberg A, Roos B, Levy B (1980) Phys Scr 21:323
28. Andersson K, Malmqvist P-Å, Roos BO, Sadlej AJ, Wolinski K (1990) J Phys Chem 94:5483
29. Andersson K, Malmqvist P-Å, Roos BO (1992) J Chem Phys 96:1218
30. Zaitsevskii A, Malrieu JP (1995) Chem Phys Lett 233:597
31. Finley J, Malmqvist P-Å, Roos BO, Serrano-Andrés L (1998) Chem Phys Lett 288:299
32. Seijo L, Barandiarán Z, Harguindey E (2001) J Chem Phys 114:118
33. Seijo L, Barandiarán Z, Ordejón B (2003) Mol Phys 101:73
34. Huzinaga S, Barandiarán Z, Seijo L, Klobukowsky M (1987) J Chem Phys 86:2132
35. Dunning TH Jr, Hay PJ (1977) In: Schaeffer HF (eds) Modern theoretical chemistry. Plenum, New York
36. Andzelm J, Klobukowsky M, Radzio-Andzelm E, Sakai Y, Tatewaki H (1984) Gaussian basis sets for molecular calculations. Elsevier, Amsterdam
37. Karlström G, Lindh R, Malmqvist P-Å, Roos BO, Ryde U, Veryazov V, Widmark P-O, Cossi M, Schimmelpfennig B, Neogrady P, Seijo L (2003) Comput Mater Sci 28:222
38. Detailed core and embedding AIMP data libraries in electronic format are available from the authors upon request or directly at the address http://www.uam.es/quimica/aimp/Data/AIMPLibs.html. See also Ref. [37]
39. Forsberg N, Malmqvist P-A (1997) Chem Phys Lett 274:196
40. Shannon RD (1976) Acta Cryst A 32:751
41. Ruipérez F, Seijo L, Barandiarán Z (2005) J Chem Phys 122:234507
42. Valiente R, Rodríguez F, González J, Güdel HU, Martín-Rodríguez R, Nataf L, Sanz-Ortiz MN, Krämer K (2009) Chem Phys Lett 481:149
43. Barandiarán Z, Seijo L (2003) J Chem Phys 119:3785
44. Pascual JL, Barros N, Barandiarán Z, Seijo L (2009) J Phys Chem A 113:12454